mater.scichina.com link.springer.com

Published online 27 October 2022 | https://doi.org/10.1007/s40843-022-2207-x
Sci China Mater 2023, 66(3): 992–1001

Post-synthetic electrostatic adsorption-assisted fabrication of efficient single-atom Fe-N-C oxygen reduction catalysts for Zn-air batteries

Le Li, Na Li, Jiawei Xia, Haoran Xing, Muhammad Arif, Yitao Zhao, Guangyu He* and Haiqun Chen*

ABSTRACT **Highly efficient platinum-group metal (PGM)-free electrocatalysts are essential for the large-scale utilization of Zn-air batteries (ZABs). Herein, we report the simple fabrication of a single atomic PGM-free electrocatalyst, Fe-SA/N-C, *via* a post-synthetic electrostatic absorption (PSEA) strategy. The single Fe atoms are anchored on the three-dimensiaonal (3D) porous carbon with adjacent N atoms, forming atomic Fe-N_4 active sites. Fe-SA/N-C exhibits excellent ORR activity in 0.1 mol L^{-1} KOH aqueous solution ($E_{1/2}$ = 0.92 V) and 0.5 mol L^{-1} H_2SO_4 aqueous solution ($E_{1/2}$ = 0.77 V), superior to those of commercial Pt/C (0.85 and 0.79 V, respectively). As a proof of concept, homemade liquid ZAB with Fe-SA/N-C catalyst displays outstanding discharging specific capacity and peak power density, outperforming the commercial Pt/C. According to the density functional theory calculation, the Fe-N_4 sites with graphitic N dopant can improve the activation of intermediates and decrease the energy barrier of the rate-determining step. This work highlights new insights for the experimental and theoretical guidance of PGM-free electrocatalysts and prescribes a general strategy for the rational design of PGM-free electrocatalysts used in ZABs.**

Keywords: 3D porous carbon, single-atom electrocatalyst, Fe-N_4 active sites, oxygen reduction reaction, zinc-air battery, density functional theory calculation

INTRODUCTION

Zn-air batteries (ZABs), a potential sustainable and environment-friendly energy conversion technology, require highly efficient electrocatalysts for the oxygen reduction reaction (ORR) process [1–5]. The platinum-group metal (PGM) catalysts have the highest kinetic activity and commercial accessibility for driving the ORR on the cathode side [6–9]. However, the high cost and scarcity of PGM catalysts restrict their widespread applications. Hence, calling for the development of low-cost, high-activity, and long-lasting alternatives to realize industrialization for ZABs is of great significance [10–14].

Among the PGM-free catalysts, the metal-nitrogen-coordinated carbon (M-N-C, M = Fe, Co, Zn, Cu, Mn, etc.) materials, especially Fe (or Co)-N-C, since their discovery in 1964, have emerged as one of the most promising substitutes [15,16]. Up to now, their encouraging ORR activity has been revealed both theoretically and experimentally [6,17–19]. The atomic Fe-N_x moieties are commonly regarded as the active sites for Fe-N-C catalysts, showing favorable ORR activity compared with that of PGM catalysts [20,21]. Recently, Fe-N_x-C single-atom catalysts (Fe-N_x-C SACs, where x is the coordination number) with maximum utilization of metal atoms and homogeneity of active sites have become a new research frontier in the catalysis community [22,23]. Generally, Fe-N_x-C SACs can be synthesized *via* direct pyrolysis of N-rich precursors with Fe salts [24–26]. However, iron species tend to aggregate during the pyrolysis process, resulting in the difficulty of removing iron-based nanoparticles or clusters, which restricts the formation of atomic Fe-N_x moieties [27]. In addition, the random mixing of the N-rich precursors with the Fe salt causes the generation of disordered pores, which hinders the access of O_2 species to the surface of Fe-N_x moieties, leading to an inferior ORR activity [28–31]. In view of this, the rational design of Fe-containing N-riched precursors at an atomic level and the synthesis of Fe-N_x-C electrocatalysts with reasonable porous structures are crucial for the enhancement of the ORR activity of ZABs.

Metal-organic frameworks (MOFs), as a class of crystalline porous materials featuring tailorable composition and structure, have been regarded as a kind of ideal precursor for the preparation of Fe-N_x-C SACs [32–37]. Despite considerable effort on the preparation of SACs, current strategies for synthesizing MOF-based Fe-N_x-C SACs are almost based on the one-step pyrolysis of targeted metal-doped MOF precursors. Nevertheless, the doped metal species may influence the construction of MOF precursors with ordered and regular morphology and structure [38,39]. Since the carbonization of MOF and the formation of single atoms occur simultaneously during the one-step pyrolysis process, the interaction effects of the raw material ratio, pyrolysis temperature, and metal loading on the formation of MOF-based Fe-N_x-C SACs remain unclear [40,41]. Hence, to gain a better understanding of the adaptability of this strategy, it is necessary to develop a simpler and clearer approach for the preparation of MOF-based Fe-N_x-C SACs with high Fe loading and fully exposed Fe-N_x active sites.

Herein, we propose a post-synthetic electrostatic absorption (PSEA) strategy to synthesize single-atom Fe (Fe-SA) catalysts anchored on three-dimensiaonal (3D) N-doped porous carbon (N-C) using Zn-MOF (zeolitic-imidazolate-frameworks-8; ZIF-8) as the sacrificial template and Fe-Phen complexes (Fe^{2+} ions coordinated with 1,10-phenanthroline) as the Fe-containing precursors. The structures of both Fe-SA/N-C and Fe-N_4 active sites were in-depth studied *via* characterization techniques assisted with density functional theory (DFT) calculation. The

Key Laboratory of Advanced Catalytic Materials and Technology, Advanced Catalysis and Green Manufacturing Collaborative Innovation Center, Changzhou University, Changzhou 213164, China
* Corresponding authors (emails: hegy@cczu.edu.cn (He G); chenhq@cczu.edu.cn (Chen H))

resultant catalyst, Fe-SA/N-C, with a high specific surface area and a composite pore structure, is conducive to exposing more active sites and facilitating the mass transfer during the electrocatalytic process, exhibiting state-of-the-art ORR activity and excellent battery performance in liquid ZABs.

EXPERIMENTAL SECTION

Chemicals

Zn (II) nitrate hexahydrate ($Zn(NO_3)_2{\cdot}6H_2O$, A.R.), ferrous acetylacetonate ($Fe(acac)_2$, A.R.), 1,10-phenanthroline (A.R.), 2-methylimidazole ($C_4H_6N_2$, A.R.), methanol (A.R.), ethanol (A.R.), and Nafion solution (5%) were purchased from Sinopharm Chemical Reagent Co. Ltd, Shanghai, China. All the chemicals and reagents were used as received without further purification unless stated otherwise, and deionized (DI) water was used throughout the whole experiment.

Synthesis of ZIF-8

In a typical procedure, 100 mL of methanol solution containing 3.57 g of $Zn(NO_3)_2{\cdot}6H_2O$ was quickly poured into another 50 mL of methanol solution containing 4.22 g of $C_4H_6N_2$ under continuous stirring. After stirring for 20 h, the white precipitate (ZIF-8) was centrifuged, washed with methanol three times, and dried in vacuum at 60°C overnight.

Synthesis of Fe/ZIF-8

In a typical procedure, Fe-Phen solution (5.18 mg of $Fe(acac)_2$ and 11.88 mg of phenanthroline (phen) dissolved in 20 mL of methanol) was ultrasonicated for 30 min before being added into 100 mL of methanol solution containing 3.57 g of $Zn(NO_3)_2{\cdot}6H_2O$ under continuous stirring for 5 h. The above suspension was quickly poured into another 50 mL of methanol solution containing 4.22 g of $C_4H_6N_2$ under continuous stirring. After stirring for 20 h, the faint yellow precipitate (Fe/ZIF-8) was centrifuged, washed with methanol three times, and dried in vacuum at 60°C overnight.

Synthesis of N-C

The obtained ZIF-8 powder ($\zeta = 20 \pm 5$ mV, ζ represents the zeta potential) was pyrolyzed at 950°C with the heating rate of 2°C min^{-1} under flowing N_2 atmosphere. After cooling down to room temperature, the powder was post-treated with 0.5 mol L^{-1} H_2SO_4 aqueous solution, washed thoroughly with DI water until neutral, and finally dried in vacuum at 60°C overnight, labelled as N-C ($\zeta = -25 \pm 5$ mV).

Synthesis of Fe-N-C

The obtained Fe/ZIF-8 powder was pyrolyzed at 950°C with the heating rate of 2°C min^{-1} under flowing N_2 atmosphere. After cooling down to room temperature, the powder was post-treated with 0.5 mol L^{-1} H_2SO_4 aqueous solution, washed thoroughly with DI water until neutral, and finally dried in vacuum at 60°C overnight, labelled as Fe-N-C.

Synthesis of Fe-SA/N-C

N-C (100 mg) was dispersed in 40 mL of methanol under sonication for 30 min. The Fe-Phen solution (5.18 mg of $Fe(acac)_2$ and 11.88 mg of phen dissolved in 20 mL of methanol) was then ultrasonicated for 30 min before being added into the above suspension under continuous stirring for 5 h. After filtration, the resultant precipitate was rinsed with DI water and dried in a vacuum oven overnight at 65°C to obtain Fe-Phen@N-C ($\zeta = -10 \pm 5$ mV). The collected sample was pyrolyzed in a tube furnace at 900°C for 3 h under N_2 atmosphere. After cooling down to room temperature, the black powder was post-treated in 0.5 mol L^{-1} H_2SO_4 aqueous solution at 80°C and then washed thoroughly with DI water until neutral. Finally, followed by drying in vacuum at 60°C overnight, Fe-SA/N-C was obtained.

Materials characterization

The morphological properties of the materials were characterized by scanning electron microscopy (SEM, Zeiss Sigma 300 Cold Field scanning electron microscope), transmission electron microscopy (TEM, JEOL JEM-2100F, performed at U_0 = 200 kV), and aberration corrector high-angle annular dark-field scanning transmission electron microscopy (AC-HAADF-STEM, FEI Theims Z, performed at 300 kV with a probe spherical aberration corrector). The crystalline structures of the materials were analyzed *via* X-ray diffraction (XRD) patterns recorded on a Rigaku Ultima IV X-ray diffractometer (Cu Kα, λ = 0.15418 nm) with the scanning range of 2θ from 10° to 80°. Raman spectra were recorded on a Thermo Fischer DXR Evolution spectrometer at a laser wavelength of 633 nm. Specific surface area and porous structure information were obtained according to N_2 adsorption-desorption isotherms performed on an AUTOSORB IQ Autosorb Brunauer-Emmett-Teller (BET) analyzer at 77 K. The chemical environment of each element was characterized by X-ray photoelectron spectroscopy (XPS, UL V AC PHI Quantera). The actual Fe content of Fe-SA/N-C was measured *via* inductively coupled plasma mass spectrometry (ICP-MS, PerkinElmer NexION 300X ICP). Atomic-level investigations of the coordination structure of the materials were conducted by X-ray absorption near-edge structure (XANES) and extended X-ray absorption fine structure (EXAFS) performed at 1W1B station in the Singapore Synchrotron Light Source (SSLS) center (operated at an energy of 2.5 GeV with an average electron current of below 200 mA).

Fabrication of home-made liquid ZABs

A clean Zn plate with a thickness of 0.6 mm was employed as the anode of liquid ZAB, and a 6 mol L^{-1} KOH aqueous solution dissolving 0.2 mol L^{-1} $Zn(Ac)_2$ was used as the electrolyte. The air electrode comprises three layers following the order of nickel foam, polyphenylene sulfide (PPS) sheet, and carbon paper, which were served as the current collector, gas diffusion layer, and catalyst carrier, respectively.

Electrochemical characterization

Electrochemical measurements for ORR and oxygen evolution reaction (OER) were conducted on a CHI 760E electrochemical potentiostat equipped with a PINE Modulated Speed Rotator, using glassy carbon electrode (GCE) and carbon rod as the working and counter electrodes, respectively. Hg/HgO and Ag/AgCl electrodes were served as the reference electrodes for alkaline medium (0.1 mol L^{-1} KOH aqueous solution) and acid medium (0.5 mol L^{-1} H_2SO_4 aqueous solution), respectively. To prepare the working electrode, freshly prepared ink composed of 3 mg of catalyst, 10 μL of 5% Nafion solution, 360 μL of ethanol, and 125 μL of DI water was carefully dropped onto the surface of GCE. After natural evaporation, a uniform layer with a catalyst

loading of 299 μg cm^{-2} was obtained. Before the measurement, the Hg/HgO electrode was calibrated to the reversible hydrogen electrode (RHE) at 25°C in 0.1 mol L^{-1} KOH aqueous solution (Fig. S1). The ORR polarization curves were recorded at room temperature in the O_2-saturated 0.1 mol L^{-1} KOH aqueous solution and 0.5 mol L^{-1} H_2SO_4 aqueous solution at various rotation rates (400–2500 r min^{-1}). Polarization curves for OER were recorded in 0.1 mol L^{-1} KOH aqueous solution at a scan rate of 5 mV s^{-1}. The potentials of the recorded polarization curves without *iR* compensation in this work were all converted to the RHE according to E(*vs.* RHE) = E(*vs.* Hg/HgO) + 0.89 V in 0.1 mol L^{-1} KOH, and E(*vs.* RHE) = E(*vs.* Ag/AgCl) +0.059 × pH + 0.196 in 0.5 mol L^{-1} H_2SO_4.

DFT calculation

All theoretical calculations were implemented based on the Vienna *Ab initio* Simulation Package (VASP). The projected-augmented wave (PAW) method was applied. The exchange-correlation energies were determined using the GGA method parameterized with the PBE functional. The Brillouin zone was sampled with Monkhorst-Pack mesh with a 2 × 2 × 1 *k*-point grid. Both geometry optimization and thermodynamic calculation were carried out with the convergence tolerance of 0.001 Å, force tolerance of 0.03 eV $Å^{-1}$, and energy tolerance of 1.0 × 10^{-5} eV.

RESULTS AND DISCUSSION

Characterizations of electrocatalysts

The synthetic procedure of the Fe-SA/N-C is illustrated in Scheme 1. ZIF-8 was first synthesized by a classical wet chemical synthetic process. Afterward, ZIF-8 was preheated at 950°C under N_2 atmosphere and then etched with H_2SO_4 aqueous solution to remove excess Zn species, resulting in a dodecahedron-shaped 3D host with a negative ζ, originating from Zn atoms volatilizing into a partial vacancy structure [42]. Consequently, the positively charged Fe-Phen complexes can be readily adsorbed into the 3D porous carbon host, thanks to the strong electrostatic interaction. The integrated precursor was then post-heated under an N_2 atmosphere and then immersed in hot acid to finally generate Fe-SA/N-C. For comparison, the reference samples obtained *via* the PSEA strategy without Fe-Phen complexes and the one-step pyrolysis are labeled as N-C and Fe-N-C, respectively. As for the synthetic precursors, detailed information on morphological and structural characterizations can be found in Figs S2–S5.

SEM and TEM images illustrate the uniform and regular rhombic dodecahedra structure of Fe-SA/N-C with a size of ~400 nm after the harsh pyrolysis process and acid etching (Fig. 1a, b and Fig. S6). High-resolution TEM (HR-TEM) observation of Fe-SA/N-C reveals no visible nanoparticles relevant to Fe-containing species on the disordered carbon matrix (Fig. 1c). The corresponding selected area electron diffraction (SAED) image displays a low crystallinity of the entire carbon framework, implying the absence of crystalline Fe species (the inset of Fig. 1c) [43]. HAADF-STEM image and the corresponding elemental mapping images demonstrate that C, N, and Fe species are homogeneously dispersed throughout the entire region, without any characteristic features of nanoclusters or nanoparticles (Fig. 1d). More importantly, AC-HAADF-STEM images clearly show numerous uniformly distributed white bright dots marked by red circles over the whole support, corresponding to Fe atoms (Fig. 1e, f) [10].

XRD pattern of Fe-SA/N-C presents two broad peaks (2θ = 24° and 43°) corresponding to (002) and (101) lattice planes of the N-doped graphitic carbon, which are identical to those of N-C and Fe-N-C (Fig. 1g) [44,45]. No Fe-containing crystalline phases can be observed due to the isolated Fe-SA feature and the low iron content (0.69 wt% measured by ICP-MS). Raman spectra of N-C and Fe-SA/N-C exhibit two peaks at 1365 and 1584 cm^{-1} (Fig. 1h), ascribed to the disordered sp^3 carbon (D band) and graphitic sp^2 carbon (G band), respectively. The intensity ratios of D and G peaks (I_D/I_G) for N-C, Fe-N-C, and Fe-SA/N-C are calculated to be 0.94, 0.93, and 0.91, respectively, suggesting the highest graphitization degree of Fe-SA/N-C [46]. N_2 adsorption-desorption isotherms of the as-synthesized catalysts exhibit a typical type-I isotherm (Fig. 1i), indicating the structures with relatively large micropores and small external surfaces in the samples [47]. Micropores are regarded as the primary host for the ORR active sites, where the adsorption of oxygen primarily occurs [48]. Fe-SA/N-C possesses a larger BET surface area (805.21 m^2 g^{-1}) than that of N-C (535.16 m^2 g^{-1}),

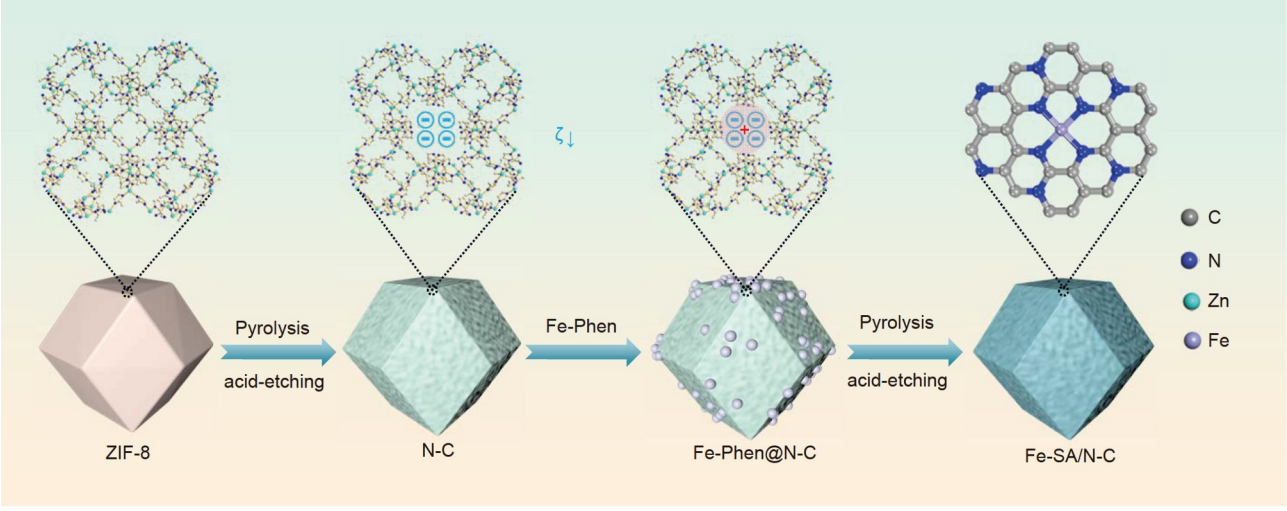

Scheme 1 Catalyst design: schematic illustration of the synthetic procedure of Fe-SA/N-C.

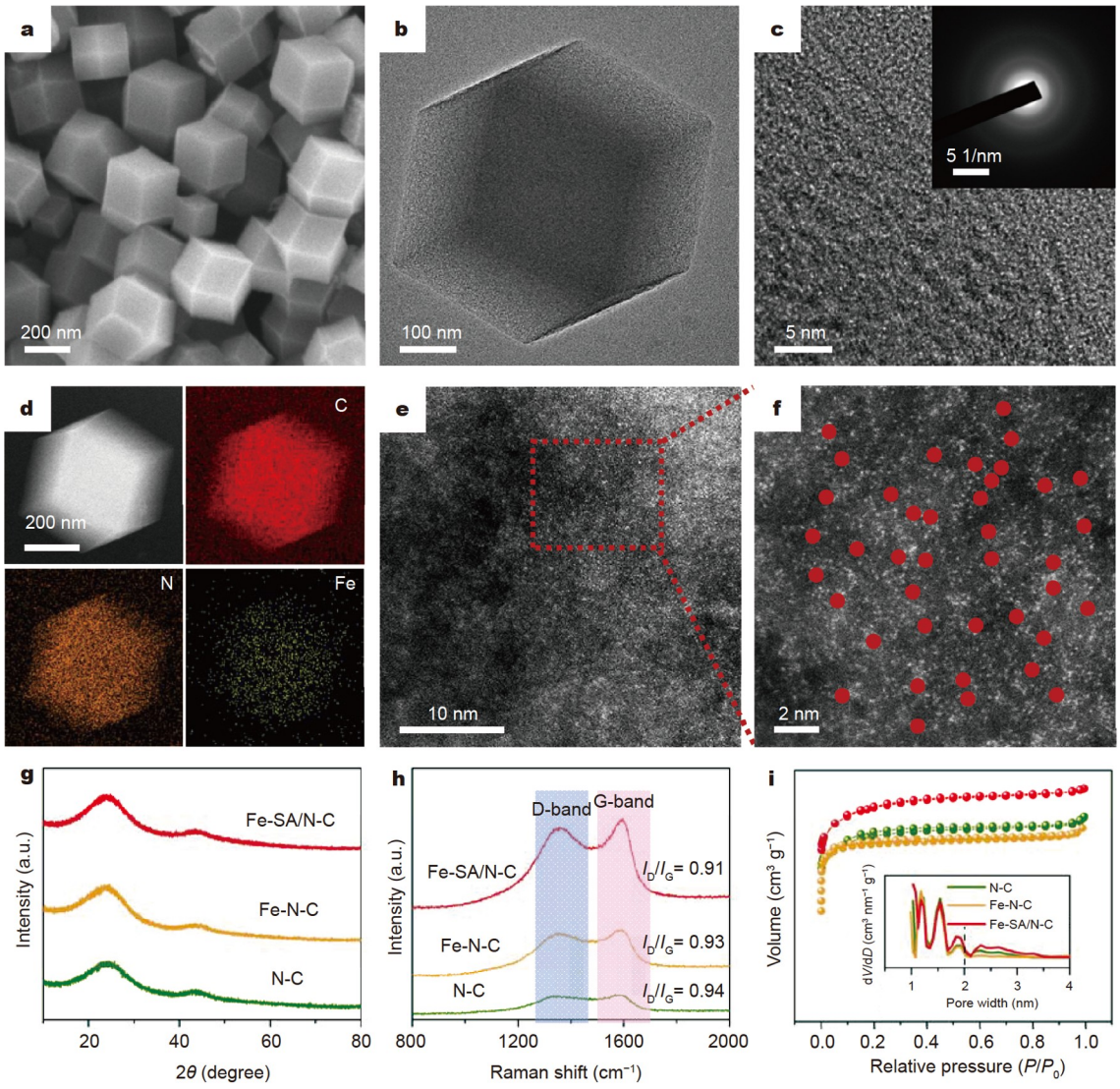

Figure 1 Morphological and structural characterizations. (a) SEM, (b) TEM, (c) HR-TEM images, and the corresponding SAED pattern of Fe-SA/N-C; (d) HAADF-TEM image of Fe-SA/N-C and the corresponding EDS maps of C (red), N (orange), and Fe (yellow); (e, f) AC-HAADF-STEM image of Fe-SA/N-C; (g) XRD patterns, (h) Raman spectra of Fe-SA/N-C, Fe-N-C, and N-C; (i) N_2 adsorption-desorption isotherm and the corresponding pore-size distribution curves (inset) of Fe-SA/N-C, Fe-N-C, and N-C.

originating from the larger micropore structure volume (0.48 $cm^3 g^{-1}$) than that of N-C (0.32 $cm^3 g^{-1}$) induced by the introduction of Fe species [49]. Since Fe species in Fe-N-C are prone to aggregate during the one-step pyrolysis process, resulting in the blockage of pores and channels. The specific surface area (424.38 $m^2 g^{-1}$) and micropore structure volume (0.27 $cm^3 g^{-1}$) of Fe-N-C are smaller than those of Fe-SA/N-C and N-C. The pore size distribution analyses (the inset of Fig. 1i) reveal the coexistence of micropores (size < 2 nm) and micro-mesopores (2 nm < size < 4 nm) in Fe-SA/N-C and N-C, allowing the accessibility of reactant molecules toward the active Fe-N_x sites for more efficient mass transfer during the electrocatalytic process [50]. Notably, such a high surface area and composite pore structure enable Fe-SA/N-C to facilitate the exposure of more Fe-N_x active sites, resulting in better ORR catalytic performance.

The C 1s XPS spectrum of Fe-SA/N-C can be resolved into C=C (~284.4 eV), C–C (~284.8 eV), C–N (~285.8 eV), and O–C=O (~288.4 eV), indicating that the heteroatom N is effectively doped into the network of porous carbon (Fig. 2a) [51,52]. As for the Fe 2p high-resolution XPS spectra of Fe-SA/N-C, the fitted peaks at ~731.83 and ~715.84 eV are assigned to the satellite peaks of Fe, while the peaks at ~712.38 eV are attributed to the Fe-N_x species (Fig. 2b). No other Fe-containing species (e.g., metallic Fe, FeO, Fe_2O_3, FeC, etc.) can be detected [53,54]. The high-resolution XPS spectra of N 1s of N-C and Fe-SA/N-C can be deconvoluted into pyridinic-N (~398.02 eV), pyrrolic-N (~399.36 eV), graphitic-N (~400.35 eV), and oxidized-N (~403.36 eV). In addition, a peak at 398.96 eV assigned to Fe-N_x species can be observed in both Fe-SA/N-C and Fe-N-C (Fig. 2c and Fig. S7), confirming the complexation effect between Fe and N species for the stabilization of single Fe atoms [55]. The graphitic N is expected to affect the geometric and electronic structures of the carbon skeleton and thus boost the intrinsic ORR activity of the Fe-N_x sites [56–58]. Fe-SA/N-C possesses a higher proportion of graphitic N than Fe-N-C

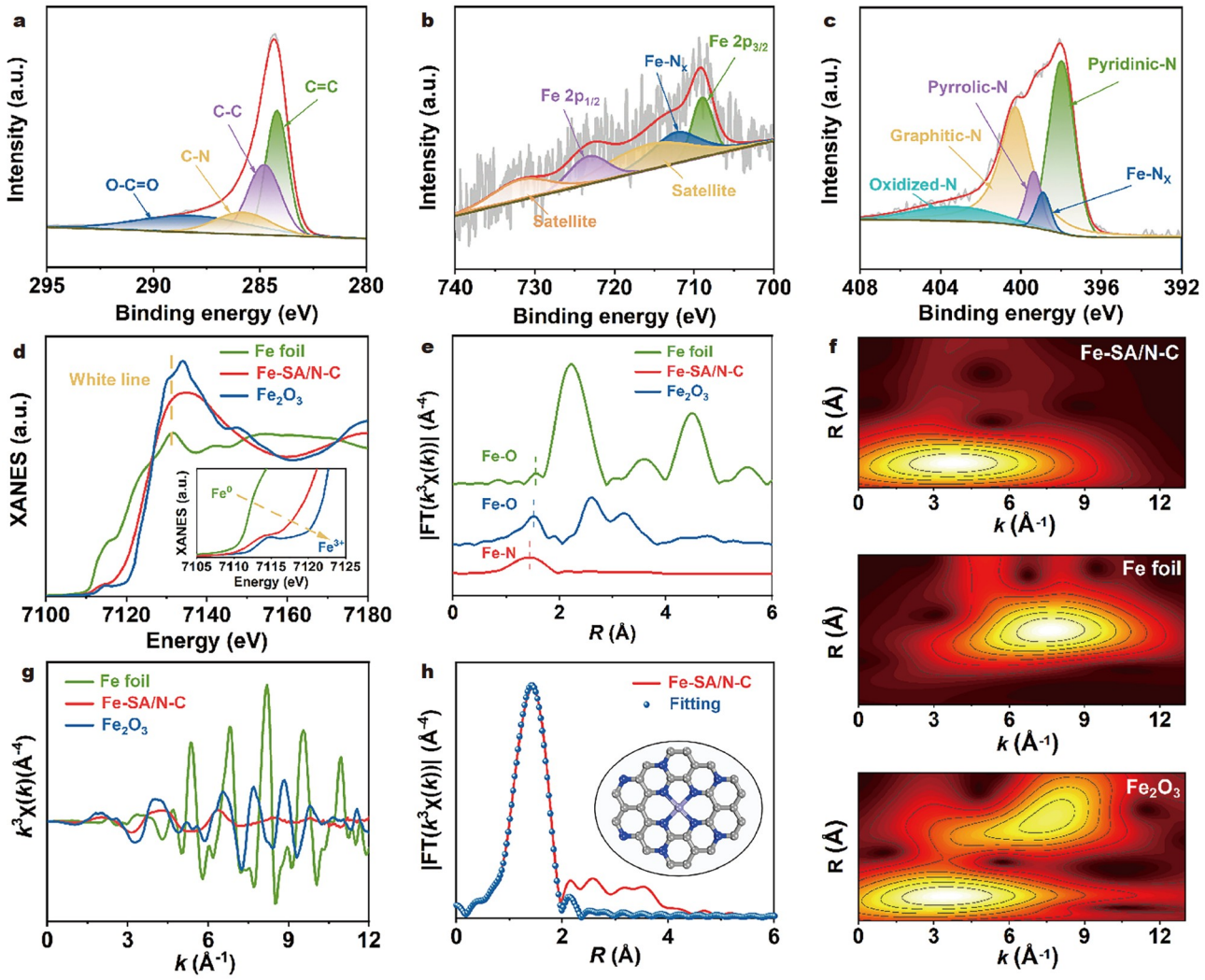

Figure 2 Structural characterizations. HRXPS spectra of (a) C 1s, (b) Fe 2p, and (c) N 1s; (d) Fe K-edge XANES spectra; (e) FT-EXAFS spectra, and (f) WT-EXAFS of the Fe K-edge of Fe-SA/NC, Fe foil and Fe_2O_3; (g) k space fitting curves of Fe-SA/NC, Fe foil and Fe_2O_3; (h) R space fitting curves of Fe-SA/NC (inset is the atomic structure model of Fe-SA/NC).

(Fig. S8 and Table S1), which is beneficial for regulating the properties of active sites. In view of the results above, we proposed a coordination structure of single Fe atoms coupled with N atoms for Fe-SA/N-C in Fig. S9. Detailed discussion for both structure analysis and ORR performance can be found as follows.

To investigate the electronic structure and coordination environment at the atomic scale, synchrotron-based X-ray absorption spectroscopy (XAS) measurements were performed on Fe-SA/N-C at the Fe K-edge [59–61]. The near-edge absorption energy of Fe-SA/N-C is located between standard Fe foil and Fe_2O_3, indicating that the oxidation state of Fe in Fe-SA/N-C is between Fe^0 and Fe^{3+} (Fig. 2d). Based on the Athena software's line combination fitting algorithm, the value of Fe^{3+}/Fe^{0+} in Fe-SA/N-C is 0.728:0.272, suggesting an average valence of 2.18 for Fe in Fe-SA/N-C. More importantly, a pre-edge peak at ~7114 eV with an additional peak at ~7131 eV can be observed in Fe-SA/N-C, which is regarded as the fingerprint of the Fe-N_4 porphyrin-like moiety [62–64]. The Fe K-edge Fourier transform (FT)-EXAFS shows the main peak at ~1.44 Å, assigned to the Fe-N configuration (Fig. 2e). No metallic Fe-Fe configuration (~2.21 Å) is detected, suggesting the existence of Fe species in the form of single atoms, which is in good agreement with the aberration-corrected HAADF-STEM result.

The wavelet transform (WT) was carried out to precisely investigate the coordination environment of Fe species in Fe-SA/N-C (Fig. 2f). The WT contour plots of Fe foil reveal a single intensity maximum at 7.8 $Å^{-1}$, which is ascribed to the Fe–Fe bond. As for Fe_2O_3, the intensity maximums at 3.4 and 7.8 $Å^{-1}$ are assigned to Fe–O and Fe–Fe bonds, respectively. Hence, referring to the above-mentioned reference samples, the single intensity maximum at ~3.8 $Å^{-1}$ in the WT contour plots of Fe-SA/N-C demonstrates Fe-N coordination for the isolated single Fe atom. EXAFS fitting was conducted to further uncover the quantitative local coordination parameters of Fe atoms (Fig 2g, h and Fig. S10, and Table S2). The coordination number of N to the central Fe atom is ~3.9, corresponding to a Fe–N bond length of ~1.96 Å, which is consistent with the optimal bond length of the model determined (1.94 Å) by DFT calculation. The fitting result of EXAFS reveals the formation of a square

planar Fe-N_4 structure (the inset of Fig. 2h).

Electrocatalytic performance toward ORR

ORR performance of the as-synthesized catalysts was evaluated by cyclic voltammetry (CV) and linear sweep voltammogram (LSV) in a 0.1 mol L^{-1} KOH aqueous solution using a rotating disk electrode (RDE). Here, typical redox peaks can be only detected in O_2-saturated electrolyte rather than in N_2-saturated electrolyte. The corresponding cathodic peaks of N-C, Fe-N-C, Fe-SA/N-C, and Pt/C are centered at ~0.74, ~0.86, ~0.91, and ~0.87 V, respectively (Fig. S11). Fe-SA/N-C prepared under the optimal conditions (Fig. S12) exhibits an E_{onset} of 1.02 V and an $E_{1/2}$ of 0.92 V (Fig. 3a, Table S3), which are much more positive than those of N-C (0.82 and 0.72 V, respectively), Fe-N-C (0.99 and 0.89 V, respectively) and commercial Pt/C (0.96 and 0.85 V, respectively). Fe-SA/N-C shows the smallest Tafel slope of 63 mV dec^{-1} (Fig. 3b) than that of N/C (119 mV dec^{-1}), Fe-N-C (85 mV dec^{-1}) and commercial Pt/C (79 mV dec^{-1}), demonstrating the fastest ORR kinetics. The kinetic current density (j_K) of Fe-SA/N-C reaches 45.81 mA cm^{-2} at 0.85 V (Fig. 3c), which is ~138.82 times that of N-C (0.33 mA cm^{-2}), ~2.86 times that of Fe-N-C (16.01 mA cm^{-2}) and ~6.89 times that of commercial Pt/C (6.65 mA cm^{-2}), respectively. The potential difference (ΔE; ΔE = $E_{1/2}$-catalyst – $E_{1/2}$-Pt/C) is applied to further assess the ORR catalytic activity [65]. Obviously, Fe-SA/N-C exhibits a high ΔE of 74 mV, which is superior to most of the reported ORR catalysts (Fig. 3d and Table S4). The linearity of Koutecky-Levich (K-L) plots derived from the ORR polarization curves at various rotation speeds reveals first-order reaction kinetics related to dissolved oxygen concentration. An electron transfer number (n) of Fe-SA/N-C calculated from K-L plots is ~3.93, approaching that of Pt/C (~4.21, the inset of Fig. 3e and Fig. S13), demonstrating a 4e⁻ oxygen reduction process in ORR. The rotating ring-disk electrode (RRDE) measurements were performed to further validate the ORR reaction pathways at the potential of 1.4 V *vs.* RHE. All the obtained catalysts exhibit a low yield of HO_2^- and a similar average n at a potential ranging from 0.2 to 0.8 V (Fig. 3f). In particular, Fe-SA/N-C shows an average n of ~3.56 with HO_2^- yield of ~4.71%, corresponding to a typical 4e⁻ ORR catalytic process.

Except for excellent ORR activity, the long-term durability of electrocatalysts is also an important parameter for the sustain-

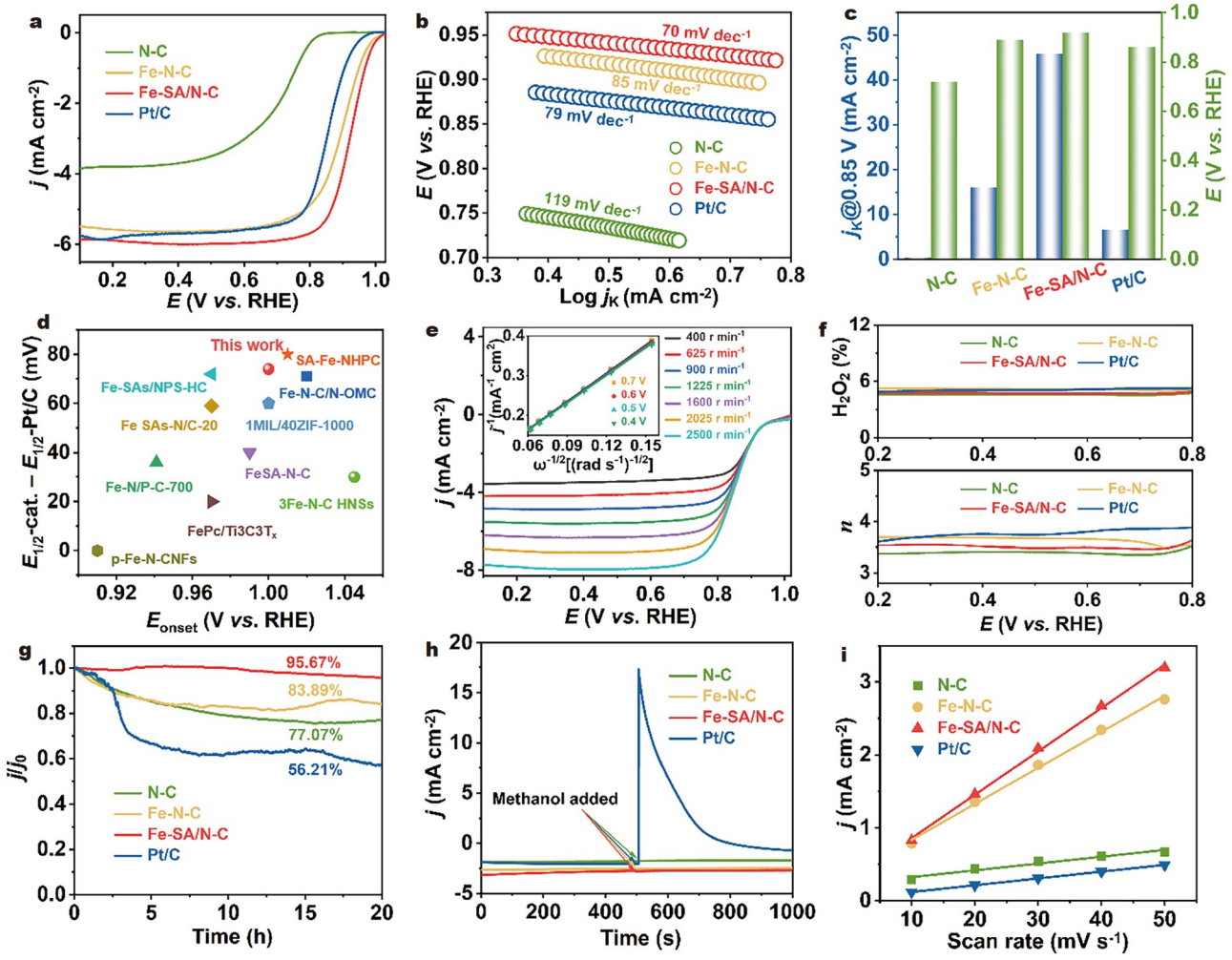

Figure 3 Electrocatalytic performance for ORR. (a) ORR polarization curves of N-C, Fe-N-C, Fe-SA/N-C, and commercial Pt/C in O_2-saturated 0.1 mol L^{-1} KOH at 1600 r min^{-1}; (b) Tafel plots, (c) j_K and $E_{1/2}$ of N-C, Fe-N-C, Fe-SA/N-C, and commercial Pt/C; (d) comparison of ΔE in this work with other representative catalysts; (e) polarization curves of Fe-SA/N-C at varied rotating speeds ranging from 400 to 2500 r min^{-1} (the inset shows the K-L plots at different potentials); (f) n and peroxide yield (%), (g) stability test, (h) methanol-tolerant test, (i) the extraction of the C_{dl} of N-C, Fe-N-C, Fe-SA/N-C, and commercial Pt/C.

able utilization of ZABs. According to the current-time curves in Fig. 3g, Fe-SA/N-C exhibits a satisfactory current density retention rate of 95.67% after 20 h in 0.1 mol L^{-1} KOH aqueous solution, which is much higher than that of N-C (77.07%), Fe-N-C (83.89%), and commercial Pt/C (56.21%), thanks to the stable chemical structure of Fe-N_4 active sites. In addition, the Fe species in Fe-SA/N-C still exist in the form of single atoms after 20 h of chronoamperometry testing (Figs S14–S17), confirming its structural and mechanical stabilities. When 0.3 mol L^{-1} methanol was added to the electrolyte for the chronoamperometry test (Fig. 3h), a substantial current change occurred over commercial Pt/C but not over other obtained samples, revealing an adequate methanol tolerance for Fe-SA/N-C, N-C, and Fe-N-C.

The double-layer capacitance (C_{dl}) calculated *via* CV measurements was conducted to evaluate the electrochemically active surface area (ECSA). The C_{dl} of Fe-SA/N-C is significantly higher than that of other reference samples (Fig. 3i and Fig. S18), owing to the combined effects of the huge specific surface area, well-ordered composite pore structure, and stable Fe-N_4 active sites of Fe-SA/N-C. In addition to the excellent ORR performance in alkaline medium discussed above, the OER activities for Fe-SA/N-C were tested in 0.1 mol L^{-1} KOH. Detailed information on OER measurements can be found in Fig. S19.

The ORR activity in acidic media is especially crucial due to its potential application in acidic proton exchange membrane fuel cells (PEMFCs). The ORR activities of the as-synthesized catalysts and commercial Pt/C were studied in 0.5 mol L^{-1} H_2SO_4 aqueous solution (Fig. S20). Here, Fe-SA/N-C displays an E_{onset} of 0.98 V and an $E_{1/2}$ of 0.77 V for ORR, which is close to those of commercial Pt/C (0.94 and 0.79 V, respectively) and higher than those of Fe-N-C (0.75 and 0.57 V, respectively, Table S5), as well as most of the non-PMG ORR electrocatalysts reported recently (Table S6). As for the reference samples, detailed information on ORR measurements in acidic medium can be found in Figs S20, S21 and Tables S5, S6.

ZAB performance

Inspired by the superior activity of Fe-SA/N-C toward ORR, we constructed a homemade liquid ZAB (LZAB@Fe-SA/N-C) using Fe-SA/N-C as the catalyst (Fig. 4a). Detailed information about the assembly of ZAB can be seen in the experimental section in the Supplementary information. Reference ZABs were also assembled for comparison by using commercial Pt/C+RuO_2 as the catalyst, labelled as LZAB@Pt/C. LZAB@Fe-SA/N-C shows a stable open-circuit voltage (OCV) of ~1.55 V, higher than that of LZAB@Fe-N-C (~1.47 V) and LZAB@Pt/C+RuO_2 (~1.49 V, Fig. 4b). Moreover, two series-wound LZAB@Fe-SA/N-Cs can power a red light-emitting diode (LED) array (3–5 V), indicating broad application prospects for the field of electronic devices (the inset of Fig. 4b). According to the long-time galvanostatic discharge at the current density of 5 mA cm^{-2} (Fig. 4c), LZAB@Fe-SA/N-C holds a superior discharge specific capacity of 800.86 mA h g^{-1} and a higher energy density of 985.06 W h kg^{-1}, compared with LZAB@Fe-N-C (728.41 mA h g^{-1}, energy density = 801.7 W h kg^{-1}, respectively), LZAB@Pt/C+RuO_2 (657.32 mA h g^{-1}, energy density = 775.61 W h kg^{-1}, respectively), and other newly reported ZABs with PGM-free catalysts (Table S7).

Particularly, the charging polarization curves were recorded in Fig. 4d. The peak power density and current density of LZAB@Fe-SA/N-C at a voltage of ~0.44 V have achieved up to 144.34 mW cm^{-2} and 325.11 mA cm^{-2}, respectively, outperforming those of LZAB@Fe-N-C (113.89 mW cm^{-2},

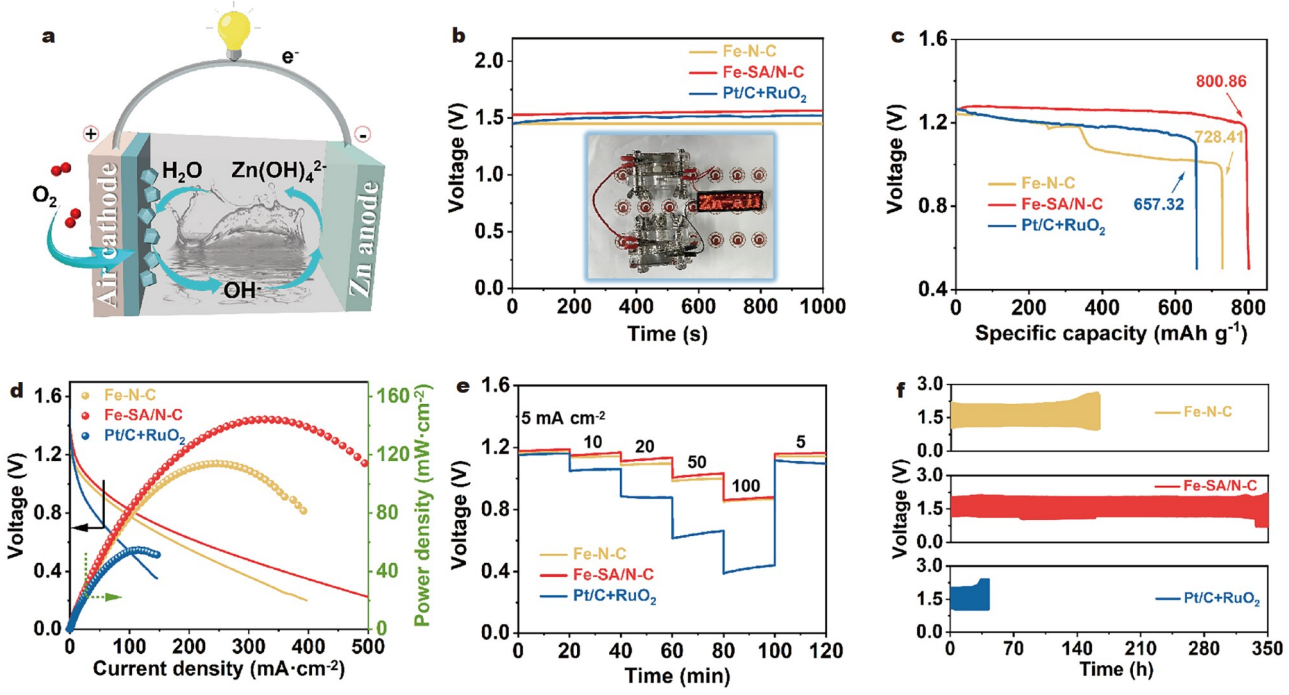

Figure 4 Electrochemical performance of liquid ZABs. (a) Schematic illustration of the mechanism of the liquid ZAB; (b) OCV curves (inset: the photograph of two LZAB@Fe-SA/N-Cs powering the red LED array); (c) voltage-specific capacity curves of LZAB@Fe-SA/N-C, LZAB@Fe-N-C and LZAB@Pt/C+RuO_2; (d) discharge polarization curves and corresponding power density curves; (e) discharge curves of ZABs at different current densities; (f) discharge-charge cycling curves at 5 mA cm^{-2} (20 min for each cycle) of liquid ZABs with Fe-N-C, Fe-SA/N-C and Pt/C+RuO_2 as the air cathode catalysts, respectively.

249.76 mA cm^{-2}, at a voltage of ~0.46 V) and LZAB@Pt/C (54.71 mW cm^{-2}, 141.46 mA cm^{-2}, at a voltage of ~0.47 V). Galvanostatic discharge observations at current densities ranging from 5 to 100 mA cm^{-2} are shown in Fig. 4e. Obviously, the discharge potential of LZAB@Fe-SA/N-C is much higher and more stable at different current densities than that of LZAB@Fe-N-C and LZAB@Pt/C. The discharge voltage of LZAB@Fe-SA/N-C can still be maintained at ~0.87 V even at 100 mA cm^{-2}, while for LZAB@Pt/C, noticeable voltage variations can be observed at 50 and 100 mA cm^{-2}, indicating excellent stability of LZAB@Fe-SA/N-C at high current densities [66]. When the current density returns to 5 mA cm^{-2}, the discharge voltage (1.16 V) of LZAB@Fe-SA/N-C still maintains 98.31% of the initial discharge voltage (1.18 V), higher than that of LZAB@Fe-N-C (1.14 V *vs.* 1.17 V, 97.43%) and LZAB@Pt/C (1.10 V *vs.* 1.16 V, 94.83%), revealing a prominent durability in the practical application. The long-term cycling tests are illustrated in Fig. 4f. LZAB@Fe-SA/N-C exhibits superior cycling stability with negligible voltage decay of up to 340 h (1020 cycles) to those of LZAB@Fe-N-C (160 h and 480 cycles, respectively) and LZAB@Pt/C (40 h and 120 cycles, respectively), which further evidences its superiority as the cathode catalyst in LZABs.

Catalytic mechanism

The mechanism underlying the enhanced catalytic activity of Fe-SA/N-C during the ORR process was studied *via* DFT calculation. Two optimized configurations were built, as shown in Fig. S22. Here, a common Fe-N$_4$ center and a Fe-N$_4$ center with graphitic N dopant nearby represent the active sites of Fe-N-C and Fe-SA/N-C, respectively. The free energy diagram for 4e$^-$ pathways on Fe-SA/N-C in an alkaline electrolyte is shown in Fig. 5a and Fig. S23.

As shown in Fig. 5b, c, at U = 0 V, both Fe-SA/N-C and Fe-N-C have the smallest absolute value of free energy change in the fourth step (desorption of *OH, $|\Delta G_4$-Fe-SA/N-C$|$ = 0.61 eV, $|\Delta G_4$-Fe-N-C$|$ = 0.37 eV, respectively), suggesting that the fourth step serves as the rate-determining step (RDS) and dominates the ORR overpotential [43]. Meanwhile, the limiting potential of Fe-SA/N-C for ORR (denoted as U_L-ORR) was calculated to be 0.61 V, which is higher than that of Fe-N-C (0.37 V). At U = 1.23 V, the RDS energy barrier required to overcome for Fe-SA/N-C is 0.62 eV, lower than that required for Fe-N-C (0.86 eV). Particularly, at U = 0.92 V ($E_{1/2}$ from electrochemical tests, Fig. 5d), the third and fourth steps of Fe-SA/N-C and Fe-N-C are both uphill, and the RDS energy barrier for Fe-SA/N-C (0.31 eV) is smaller than that for Fe-N-C (0.55 eV), in agreement with the electrochemical test results. All the results above further verify the high activity of the Fe-N$_4$ center with graphitic N dopants that can decrease the energy barrier of the RDS and thus accelerate the ORR process.

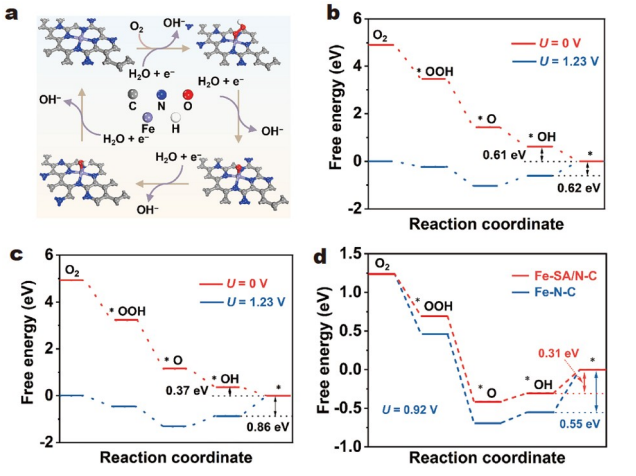

Figure 5 Theoretical calculation. (a) Scheme of the transition states in the mechanism of ORR at Fe-SA/N-C from DFT; free energy diagrams of different ORR intermediates *OOH, *O, and *OH at 0 and 1.23 V for (b) Fe-SA/N-C and (c) Fe-N-C; (d) free energy diagrams of Fe-SA/N-C (red) and Fe-N-C (ink blue) at 0.92 V.

CONCLUSIONS

In summary, we propose a simple PSEA strategy to synthesize an atomically dispersed Fe-N$_4$ catalyst anchored on N-doped 3D porous carbon. The atomic Fe-N$_4$ moiety with adjacent graphitic N dopants can effectively promote the generation of reactive intermediates and decrease the energy barrier for the RDS, thus accelerating the intrinsic ORR processes. The resultant catalyst, Fe-SA/N-C, shows outstanding ORR performance in terms of high onset potential (1.02 V in 0.1 mol L^{-1} KOH aqueous solution, 0.98 V in 0.5 mol L^{-1} H_2SO_4 aqueous solution, respectively), half-wave potential (0.92 V in 0.1 mol L^{-1} KOH aqueous solution, 0.77 V in 0.5 mol L^{-1} H_2SO_4 aqueous solution, respectively), high kinetic current density (45.81 mA cm^{-2}@0.85 V in 0.1 mol L^{-1} KOH aqueous solution, 4.26 mA cm^{-2}@0.75 V in 0.5 mol L^{-1} H_2SO_4 aqueous solution, respectively), excellent stability, and methanol resistance. Notably, the homemade liquid ZAB assembled with Fe-SA/N-C as the catalyst exhibits remarkable battery performance in terms of high OCV (~1.55 V), potential specific capacity (800.86 mA h g^{-1}), peak power density (144.34 mW cm^{-2}), and excellent discharge voltage retention rate at high current densities (98.31%). The combination of experimental results and mechanism studies reveals that the outstanding ORR activity stems from: (1) enhanced intrinsic activity of Fe-N$_4$ with adjacent graphitic N dopants; (2) high surface area and composite pore structure that is beneficial for the accessibility of reactant molecules toward active sites. This work provides a new idea for designing and synthesizing highly efficient PGM-free electrocatalysts for ORR.

Received 31 May 2022; accepted 25 July 2022; published online 27 October 2022

1 Wang HF, Tang C, Zhang Q. A review of precious-metal-free bifunctional oxygen electrocatalysts: Rational design and applications in Zn-air batteries. Adv Funct Mater, 2018, 28: 1803329
2 Zhou T, Zhang N, Wu C, *et al.* Surface/interface nanoengineering for rechargeable Zn-air batteries. Energy Environ Sci, 2020, 13: 1132–1153
3 Sun Q, Zhu K, Ji X, *et al.* MOF-derived three-dimensional ordered porous carbon nanomaterial for efficient alkaline zinc-air batteries. Sci China Mater, 2022, 65: 1453–1462
4 Wang Y, Wang L, Fu H. Research progress of Fe-N-C catalysts for the electrocatalytic oxygen reduction reaction. Sci China Mater, 2022, 65: 1701–1722
5 Han S, Chen Y, Hao Y, *et al.* Multi-dimensional hierarchical CoS_2@MXene as trifunctional electrocatalysts for zinc-air batteries and overall water splitting. Sci China Mater, 2021, 64: 1127–1138
6 Zhang Z, Sun J, Wang F, *et al.* Efficient oxygen reduction reaction (ORR) catalysts based on single iron atoms dispersed on a hierarchically structured porous carbon framework. Angew Chem Int Ed, 2018, 57: 9038–9043

7 Tan F, Li W, Wang J, *et al.* Clarifying the critical roles of iron in boosting oxygen reduction: Single Fe atoms anchored on carbon vacancies as efficient active sites. Appl Catal B-Environ, 2022, 305: 121035
8 Li Q, Chen W, Xiao H, *et al.* Fe isolated single atoms on S, N codoped carbon by copolymer pyrolysis strategy for highly efficient oxygen reduction reaction. Adv Mater, 2018, 30: 1800588
9 Xiao F, Xu GL, Sun CJ, *et al.* Nitrogen-coordinated single iron atom catalysts derived from metal organic frameworks for oxygen reduction reaction. Nano Energy, 2019, 61: 60–68
10 Yu D, Ma Y, Hu F, *et al.* Dual-sites coordination engineering of single atom catalysts for flexible metal-air batteries. Adv Energy Mater, 2021, 11: 2101242
11 Li L, Yu D, Li P, *et al.* Interfacial electronic coupling of ultrathin transition-metal hydroxide nanosheets with layered MXenes as a new prototype for platinum-like hydrogen evolution. Energy Environ Sci, 2021, 14: 6419–6427
12 Deng L, Hu F, Ma M, *et al.* Electronic modulation caused by interfacial Ni-O-M (M = Ru, Ir, Pd) bonding for accelerating hydrogen evolution kinetics. Angew Chem Int Ed, 2021, 60: 22276–22282
13 Huang H, Yu D, Hu F, *et al.* Clusters induced electron redistribution to tune oxygen reduction activity of transition metal single-atom for metal-air batteries. Angew Chem, 2022, 134: e202116068
14 Hu F, Yu D, Ye M, *et al.* Lattice-matching formed mesoporous transition metal oxide heterostructures advance water splitting by active Fe–O–Cu bridges. Adv Energy Mater, 2022, 12: 2200067
15 Wang A, Li J, Zhang T. Heterogeneous single-atom catalysis. Nat Rev Chem, 2018, 2: 65–81
16 Pan Y, Liu S, Sun K, *et al.* A bimetallic Zn/Fe polyphthalocyanine-derived single-atom Fe-N_4 catalytic site: A superior trifunctional catalyst for overall water splitting and Zn-air batteries. Angew Chem, 2018, 130: 8750–8754
17 Chen Y, Ji S, Wang Y, *et al.* Isolated single iron atoms anchored on N-doped porous carbon as an efficient electrocatalyst for the oxygen reduction reaction. Angew Chem Int Ed, 2017, 56: 6937–6941
18 Hou CC, Zou L, Sun L, *et al.* Single-atom iron catalysts on overhanging carbon cages for high-performance oxygen reduction reaction. Angew Chem Int Ed, 2020, 59: 7384–7389
19 Liu D, Li J, Ding S, *et al.* 2D single-atom catalyst with optimized iron sites produced by thermal melting of metal-organic frameworks for oxygen reduction reaction. Small Methods, 2020, 4: 1900827
20 Zhu C, Shi Q, Xu BZ, *et al.* Hierarchically porous M-N-C (M = Co and Fe) single-atom electrocatalysts with robust MN_x active moieties enable enhanced ORR performance. Adv Energy Mater, 2018, 8: 1801956
21 Wei H, Liu X, Wang A, *et al.* FeO_x-supported platinum single-atom and pseudo-single-atom catalysts for chemoselective hydrogenation of functionalized nitroarenes. Nat Commun, 2014, 5: 5634
22 He Y, Liu S, Priest C, *et al.* Atomically dispersed metal-nitrogen-carbon catalysts for fuel cells: Advances in catalyst design, electrode performance, and durability improvement. Chem Soc Rev, 2020, 49: 3484–3524
23 Wang Q, Yang Y, Sun F, *et al.* Molten NaCl-assisted synthesis of porous Fe-N-C electrocatalysts with a high density of catalytically accessible FeN_4 active sites and outstanding oxygen reduction reaction performance. Adv Energy Mater, 2021, 11: 2100219
24 Wu L, Ni B, Chen R, *et al.* A general approach for hierarchically porous metal/N/C nanosphere electrocatalysts: Nano-confined pyrolysis of *in situ*-formed amorphous metal-ligand complexes. J Mater Chem A, 2020, 8: 21026–21035
25 Song Z, Zhang L, Doyle-Davis K, *et al.* Recent advances in MOF-derived single atom catalysts for electrochemical applications. Adv Energy Mater, 2020, 10: 2001561
26 Han A, Wang X, Tang K, *et al.* An adjacent atomic platinum site enables single-atom iron with high oxygen reduction reaction performance. Angew Chem Int Ed, 2021, 60: 19262–19271
27 Qiao Y, Yuan P, Hu Y, *et al.* Sulfuration of an Fe-N-C catalyst containing Fe_xC/Fe species to enhance the catalysis of oxygen reduction in acidic media and for use in flexible Zn-Air batteries. Adv Mater, 2018, 30: 1804504
28 Xia BY, Yan Y, Li N, *et al.* A metal-organic framework-derived bifunctional oxygen electrocatalyst. Nat Energy, 2016, 1: 15006
29 Han Y, Wang YG, Chen W, *et al.* Hollow N-doped carbon spheres with isolated cobalt single atomic sites: Superior electrocatalysts for oxygen reduction. J Am Chem Soc, 2017, 139: 17269–17272
30 Shen H, Gracia-Espino E, Ma J, *et al.* Atomically FeN_2 moieties dispersed on mesoporous carbon: A new atomic catalyst for efficient oxygen reduction catalysis. Nano Energy, 2017, 35: 9–16
31 Joo SH, Choi SJ, Oh I, *et al.* Ordered nanoporous arrays of carbon supporting high dispersions of platinum nanoparticles. Nature, 2001, 412: 169–172
32 Wei YS, Zhang M, Zou R, *et al.* Metal-organic framework-based catalysts with single metal sites. Chem Rev, 2020, 120: 12089–12174
33 Qiu T, Liang Z, Guo W, *et al.* Metal-organic framework-based materials for energy conversion and storage. ACS Energy Lett, 2020, 5: 520–532
34 Cai G, Yan P, Zhang L, *et al.* Metal-organic framework-based hierarchically porous materials: Synthesis and applications. Chem Rev, 2021, 121: 12278–12326
35 Li L, Chen YJ, Xing HR, *et al.* Single-atom Fe-N_5 catalyst for high-performance zinc-air batteries. Nano Res, 2022, 15: 8056–8064
36 Jiao L, Jiang HL. Metal-organic-framework-based single-atom catalysts for energy applications. Chem, 2019, 5: 786–804
37 Xie X, Peng L, Yang H, *et al.* MIL-101-derived mesoporous carbon supporting highly exposed Fe single-atom sites as efficient oxygen reduction reaction catalysts. Adv Mater, 2021, 33: 2101038
38 Wang X, Chen Z, Zhao X, *et al.* Regulation of coordination number over single Co sites: Triggering the efficient electroreduction of CO_2. Angew Chem Int Ed, 2018, 57: 1944–1948
39 Pan Y, Chen Y, Wu K, *et al.* Regulating the coordination structure of single-atom Fe-N_xC_y catalytic sites for benzene oxidation. Nat Commun, 2019, 10: 4290
40 Yan C, Li H, Ye Y, *et al.* Coordinatively unsaturated nickel-nitrogen sites towards selective and high-rate CO_2 electroreduction. Energy Environ Sci, 2018, 11: 1204–1210
41 Li X, Rong H, Zhang J, *et al.* Modulating the local coordination environment of single-atom catalysts for enhanced catalytic performance. Nano Res, 2020, 13: 1842–1855
42 Wan X, Liu X, Li Y, *et al.* Fe–N–C electrocatalyst with dense active sites and efficient mass transport for high-performance proton exchange membrane fuel cells. Nat Catal, 2019, 2: 259–268
43 Han J, Bao H, Wang JQ, *et al.* 3D N-doped ordered mesoporous carbon supported single-atom Fe-N-C catalysts with superior performance for oxygen reduction reaction and zinc-air battery. Appl Catal B-Environ, 2021, 280: 119411
44 Han J, Meng X, Lu L, *et al.* Single-atom Fe-N_x-C as an efficient electrocatalyst for zinc-air batteries. Adv Funct Mater, 2019, 29: 1808872
45 Ao X, Zhang W, Li Z, *et al.* Markedly enhanced oxygen reduction activity of single-atom Fe catalysts *via* integration with Fe nanoclusters. ACS Nano, 2019, 13: 11853–11862
46 Li P, Qi X, Zhao L, *et al.* Hierarchical 3D porous carbon with facilely accessible Fe-N_4 single-atom sites for Zn-air batteries. J Mater Chem A, 2022, 10: 5925–5929
47 Leofanti G, Padovan M, Tozzola G, *et al.* Surface area and pore texture of catalysts. Catal Today, 1998, 41: 207–219
48 Jaouen F, Lefèvre M, Dodelet JP, *et al.* Heat-treated Fe/N/C catalysts for O_2 electroreduction: Are active sites hosted in micropores? J Phys Chem B, 2006, 110: 5553–5558
49 Tian P, Liu D, Li K, *et al.* Porous metal-organic framework $Cu_3(BTC)_2$ as catalyst used in air-cathode for high performance of microbial fuel cell. Bioresource Tech, 2017, 244: 206–212
50 Chen G, Wang T, Liu P, *et al.* Promoted oxygen reduction kinetics on nitrogen-doped hierarchically porous carbon by engineering proton-feeding centers. Energy Environ Sci, 2020, 13: 2849–2855
51 Zheng L, Yu S, Lu X, *et al.* Two-dimensional bimetallic Zn/Fe-metal-organic framework (MOF)-derived porous carbon nanosheets with a high density of single/paired Fe atoms as high-performance oxygen reduction catalysts. ACS Appl Mater Interfaces, 2020, 12: 13878–13887
52 Jiao L, Wan G, Zhang R, *et al.* From metal-organic frameworks to single-atom Fe implanted N-doped porous carbons: Efficient oxygen reduction in both alkaline and acidic media. Angew Chem Int Ed, 2018,

57: 8525–8529
53 Wang H, Yin F, Liu N, *et al.* Engineering Fe-Fe_3C@Fe-N-C active sites and hybrid structures from dual metal-organic frameworks for oxygen reduction reaction in H_2-O_2 fuel cell and Li-O_2 battery. Adv Funct Mater, 2019, 29: 1901531
54 Jiang WJ, Gu L, Li L, *et al.* Understanding the high activity of Fe-N-C electrocatalysts in oxygen reduction: Fe/Fe_3C nanoparticles boost the activity of Fe-N_x. J Am Chem Soc, 2016, 138: 3570–3578
55 Cheng N, Li JC, Liu D, *et al.* Single-atom nanozyme based on nanoengineered Fe-N-C catalyst with superior peroxidase-like activity for ultrasensitive bioassays. Small, 2019, 15: 1901485
56 Zhu J, Zhou H, Zhang C, *et al.* Dual active nitrogen doped hierarchical porous hollow carbon nanospheres as an oxygen reduction electrocatalyst for zinc-air batteries. Nanoscale, 2017, 9: 13257–13263
57 Zhao Y, Lai Q, Wang Y, *et al.* Interconnected hierarchically porous Fe, N-codoped carbon nanofibers as efficient oxygen reduction catalysts for Zn-Air batteries. ACS Appl Mater Interfaces, 2017, 9: 16178–16186
58 Huang H, Yan M, Yang C, *et al.* Graphene nanoarchitectonics: Recent advances in graphene-based electrocatalysts for hydrogen evolution reaction. Adv Mater, 2019, 31: 1903415
59 Ravel B, Newville M. *ATHENA*, *ARTEMIS*, *HEPHAESTUS*: Data analysis for X-ray absorption spectroscopy using *IFEFFIT*. J Synchrotron Rad, 2005, 12: 537–541
60 Funke H, Chukalina M, Rossberg A. Wavelet analysis of extended X-ray absorption fine structure data. Phys Scripta, 2005, 2005: 232
61 Zabinsky SI, Rehr JJ, Ankudinov A, *et al.* Multiple-scattering calculations of X-ray-absorption spectra. Phys Rev B, 1995, 52: 2995–3009
62 Chen X, Ma DD, Chen B, *et al.* Metal-organic framework-derived mesoporous carbon nanoframes embedded with atomically dispersed Fe–N active sites for efficient bifunctional oxygen and carbon dioxide electroreduction. Appl Catal B-Environ, 2020, 267: 118720
63 Chen Y, Li Z, Zhu Y, *et al.* Atomic Fe dispersed on N-doped carbon hollow nanospheres for high-efficiency electrocatalytic oxygen reduction. Adv Mater, 2019, 31: 1806312
64 Wang YC, Wan LY, Cui PX, *et al.* Porous carbon membrane-supported atomically dispersed pyrrole-type Fe-N_4 as active sites for electrochemical hydrazine oxidation reaction. Small, 2020, 16: 2002203
65 Deng Y, Chi B, Tian X, *et al.* g-C_3N_4 promoted MOF derived hollow carbon nanopolyhedra doped with high density/fraction of single Fe atoms as an ultra-high performance non-precious catalyst towards acidic ORR and PEM fuel cells. J Mater Chem A, 2019, 7: 5020–5030
66 Sun T, Zang W, Yan H, *et al.* Engineering the coordination environment of single cobalt atoms for efficient oxygen reduction and hydrogen evolution reactions. ACS Catal, 2021, 11: 4498–4509

Acknowledgements This work was supported by the National Natural Science Foundation of China (22078028 and 21978026). The authors would like to thank the Shiyanjia lab (www.shiyanjia.com) for materials characterization, Prof. Yin for the support of VASP software, and Changzhou University Computer Center for computing services.

Author contributions Li L designed the research. Li L and Li N performed the experiments and wrote the original draft. Xing H conducted the model optimization and performed DFT calculations. Li L, Xia J, Arif M, and Zhao Y made formal analysis and editing. He G and Chen H supervised the research.

Conflict of interest The authors declare that they have no conflict of interest.

Supplementary information Experimental details and supporting data are available in the online version of the paper.

Le Li received his master degree from Changzhou University in 2018, and now he is a PhD student at Changzhou University. His current research focuses on the design and synthesis of single-atom catalysts for electrochemical applications.

Guangyu He is a professor at Changzhou University. She received her PhD degree from Nanjing University of Science and Technology. Her research mainly focuses on graphene-based functional materials for applications in advanced energy storage materials and devices and environmental engineering.

Haiqun Chen is a professor at Changzhou University. He received his PhD degree from Nanjing University of Science and Technology. His research mainly focuses on graphene-based functional materials for applications in environmental engineering, catalytic chemistry, and supercapacitors.

后合成静电吸附辅助制备高效Fe-N-C单原子氧还原催化剂用于锌-空气电池

李乐, 李娜, 夏佳伟, 邢浩然, 阿里夫·默罕默德, 赵宜涛, 何光裕*, 陈海群*

摘要 设计和制备高效的非铂族催化剂对锌-空气电池的大规模应用至关重要. 本文采用简单的后合成静电吸附策略制备了Fe-N-C单原子催化剂(Fe-SA/N-C). 其中, Fe原子与相邻的氮原子形成Fe-N_4活性位点并锚定在三维多孔碳上. 该催化剂在0.1 mol L^{-1} KOH ($E_{1/2}$ = 0.92 V)和0.5 mol L^{-1} H_2SO_4 ($E_{1/2}$ = 0.77 V)中均表现出优异的氧化还原活性, 性能优于商业Pt/C催化剂(0.1 mol L^{-1} KOH, $E_{1/2}$ = 0.85 V; 0.5 mol L^{-1} H_2SO_4, $E_{1/2}$ = 0.79 V). 此外, 以Fe-SA/N-C作为阴极催化剂自组装的液体锌-空气电池具有优异的放电比容量和峰值功率密度, 优于商业Pt/C催化剂. 密度泛函理论计算结果表明, 石墨化氮掺杂的Fe-N_4位点能有效提高ORR中间产物的活化程度, 降低速率决定步骤的能垒. 本工作对非铂族催化剂的实验制备和理论研究提出了新的见解, 为锌-空气电池中使用的非铂族催化剂的合理设计提供了一般策略.

